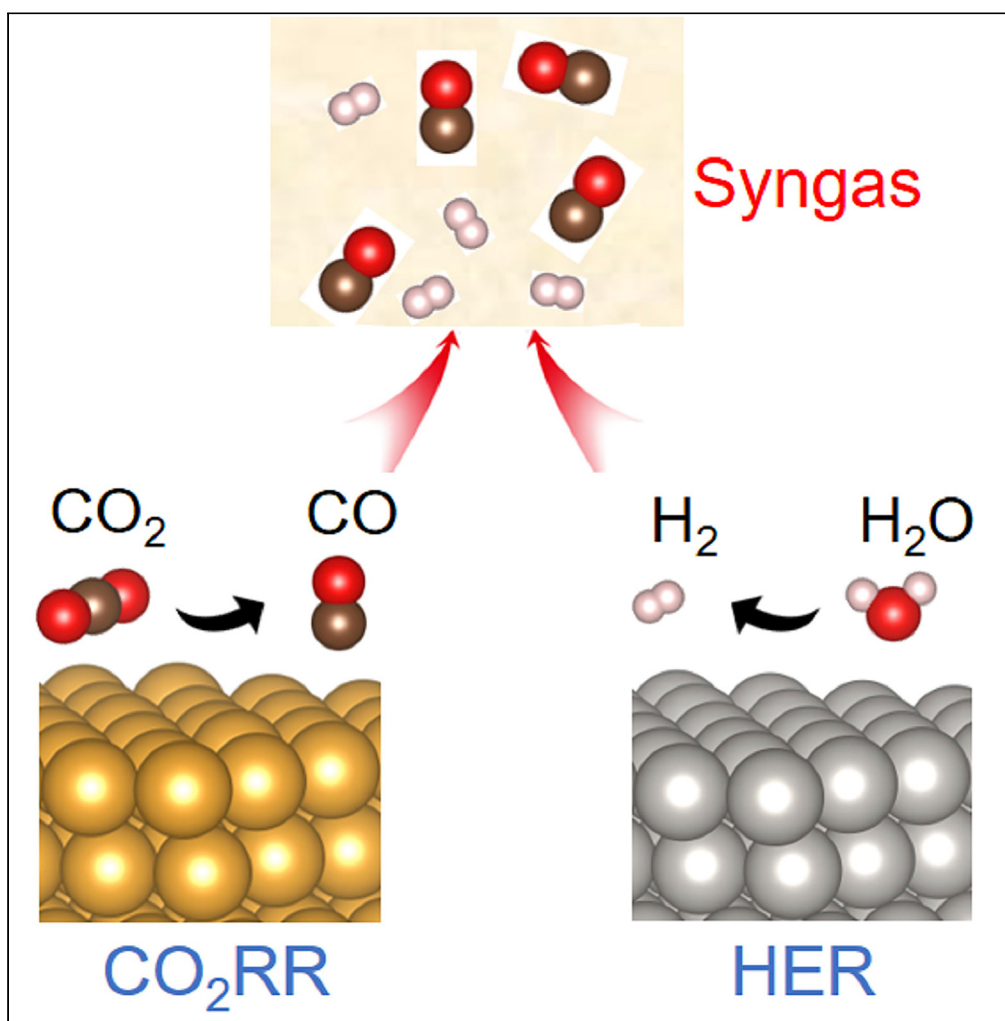


Article

Decoupling Strategy for Enhanced Syngas Generation from Photoelectrochemical CO₂ Reduction

Sheng Chu,
Pengfei Ou,
Roksana Tonny
Rashid, ..., Huiyan
Zhang, Jun Song,
Zetian Mi

schu@seu.edu.cn (S.C.)
jun.song2@mcgill.ca (J.S.)
ztmi@umich.edu (Z.M.)

HIGHLIGHTS
Combined experimental
and theoretical
investigations were
performed

A record high applied bias
photon-to-current
efficiency of 1.88% was
achieved

The CO/H₂ ratio in the
syngas product can be
controllably tuned in a
wide range

Unassisted syngas
generation was proved in
a tandem
photoelectrochemical cell

Chu et al., iScience 23, 101390
August 21, 2020 © 2020 The
Author(s).
<https://doi.org/10.1016/j.isci.2020.101390>



Article

Decoupling Strategy for Enhanced Syngas Generation from Photoelectrochemical CO₂ Reduction

Sheng Chu,^{1,2,5,*} Pengfei Ou,^{3,5} Roksana Tonny Rashid,^{2,5} Pegah Ghamari,^{2,5} Renjie Wang,² Hong Nhung Tran,² Songrui Zhao,² Huiyan Zhang,¹ Jun Song,^{3,*} and Zetian Mi^{2,4,6,*}

SUMMARY

Photoelectrochemical CO₂ reduction into syngas (a mixture of CO and H₂) provides a promising route to mitigate greenhouse gas emissions and store intermittent solar energy into value-added chemicals. Design of photoelectrode with high energy conversion efficiency and controllable syngas composition is of central importance but remains challenging. Herein, we report a decoupling strategy using dual cocatalysts to tackle the challenge based on joint computational and experimental investigations. Density functional theory calculations indicate the optimization of syngas generation using a combination of fundamentally distinctive catalytic sites. Experimentally, by integrating spatially separated dual cocatalysts of a CO-generating catalyst and a H₂-generating catalyst with GaN nanowires on planar Si photocathode, we report a record high applied bias photon-to-current efficiency of 1.88% and controllable syngas products with tunable CO/H₂ ratios (0–10) under one-sun illumination. Moreover, unassisted solar CO₂ reduction with a solar-to-syngas efficiency of 0.63% is demonstrated in a tandem photoelectrochemical cell.

INTRODUCTION

Photoelectrochemical (PEC) CO₂ reduction represents a promising route to store intermittent solar energy into clean and sustainable chemical fuels, while simultaneously reducing atmospheric carbon emissions at ambient conditions (White et al., 2015; Zhang et al., 2018; Shan et al., 2019; Feng et al., 2020; Zhou et al., 2020). In aqueous solutions, CO₂ reduction reaction (CO₂RR) is difficult to compete with hydrogen evolution reaction (HER), since HER is kinetically more feasible owing to a two-electron transfer process and the high proton concentration in aqueous environment (Zhang et al., 2014; Qiu et al., 2015; Landers et al., 2018). In this context, the generation of syngas (a mixture of CO and H₂) from a combination of CO₂RR and HER renders the opportunity to utilize side product H₂ and leverages well-established industrial processes (e.g., Fischer-Tropsch technology) for synthesizing long hydrocarbons and liquid fuels (Sheng et al., 2017).

In practical applications to upgrade syngas into downstream products, the ratio of CO/H₂ plays a key role in tuning the product selectivity (e.g., 1:1, 1:2, and 1:3 for hydroformylation, methanol synthesis, and methanation reaction, respectively) (Kang et al., 2014; Foit et al., 2017; He et al., 2018; Ross et al., 2019; Lee et al., 2019). In industrial technology, the CO/H₂ ratio was adjusted by use of the (reverse) water-gas shift process, which is costly and has a large carbon footprint. Therefore, it is desirable to develop an efficient PEC syngas generation system that can deliver controllable CO/H₂ ratio. To date, a variety of photocathodes, such as p-Si (Kong et al., 2016; Song et al., 2017; Chu et al., 2016, 2018; Li et al., 2019), ZnTe (Jang et al., 2014, 2015), Cu₂O (Schreier et al., 2015b; Deng et al., 2019b), and perovskite (Andrei et al., 2020), usually in conjunction with a CO₂RR cocatalyst (e.g., Au, Ag, and molecular metal-complex), have been developed for PEC CO₂ reduction into CO/syngas. However, it remains challenging to develop efficient syngas production with widely controllable CO/H₂ ratio, as a single catalyst with a monofunctional site usually cannot provide balanced and simultaneously optimized CO₂RR and HER activity. Herein, we report a decoupling strategy using spatially separated dual cocatalysts to tackle the challenge, on the basis of theoretical calculations and experimental verifications. By rationally assembling a Au CO-generating site and a Pt H₂-generating site at the tip and side of GaN nanowires, respectively, a record high applied bias photon-to-current efficiency (ABPE) of 1.88% was achieved on planar Si photocathode. In addition, the CO/H₂ ratio in the syngas

¹Key Laboratory of Energy Thermal Conversion and Control of Ministry of Education, School of Energy and Environment, Southeast University, Nanjing 210096, China

²Department of Electrical and Computer Engineering, McGill University, 3480 University Street, Montreal, QC H3A 0E9, Canada

³Department of Mining and Materials Engineering, McGill University, 3610 University Street, Montreal, QC H3A 0C5, Canada

⁴Department of Materials Science and Engineering, University of Michigan, Ann Arbor, 1301 Beal Avenue, Ann Arbor, MI 48109, USA

⁵These authors contributed equally

⁶Lead Contact

*Correspondence:
schu@seu.edu.cn (S.C.),
jun.song2@mcgill.ca (J.S.),
ztm@umich.edu (Z.M.)

<https://doi.org/10.1016/j.isci.2020.101390>



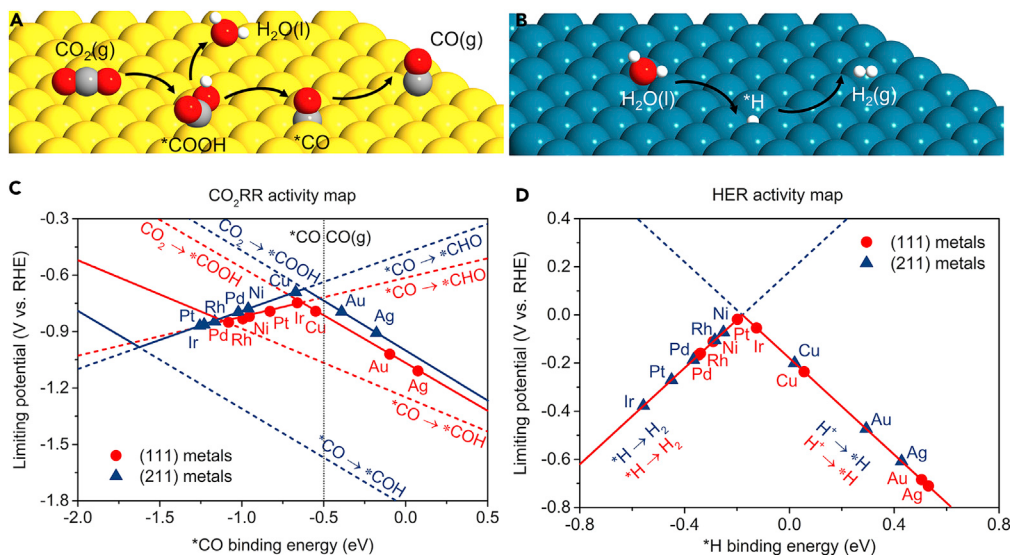


Figure 1. Theory-Guided Design of Enhanced Syngas Generation by Decoupling Strategy

Schematic of reaction paths for (A) CO₂RR to CO and (B) HER. Theoretical predicted volcano plots of (C) CO₂RR activity versus *CO binding energy and (D) HER activity versus *H binding energy on (111) and (211) facets of different fcc metals. The black vertical dashed line shows the equilibrium potential of *CO/CO. Red and blue solid lines show the potential-limiting steps for CO₂RR and HER as the *CO/*H binding energy varies on the (111) and (211) facets, respectively, whereas dashed lines show associated elementary steps for CO₂RR and HER.

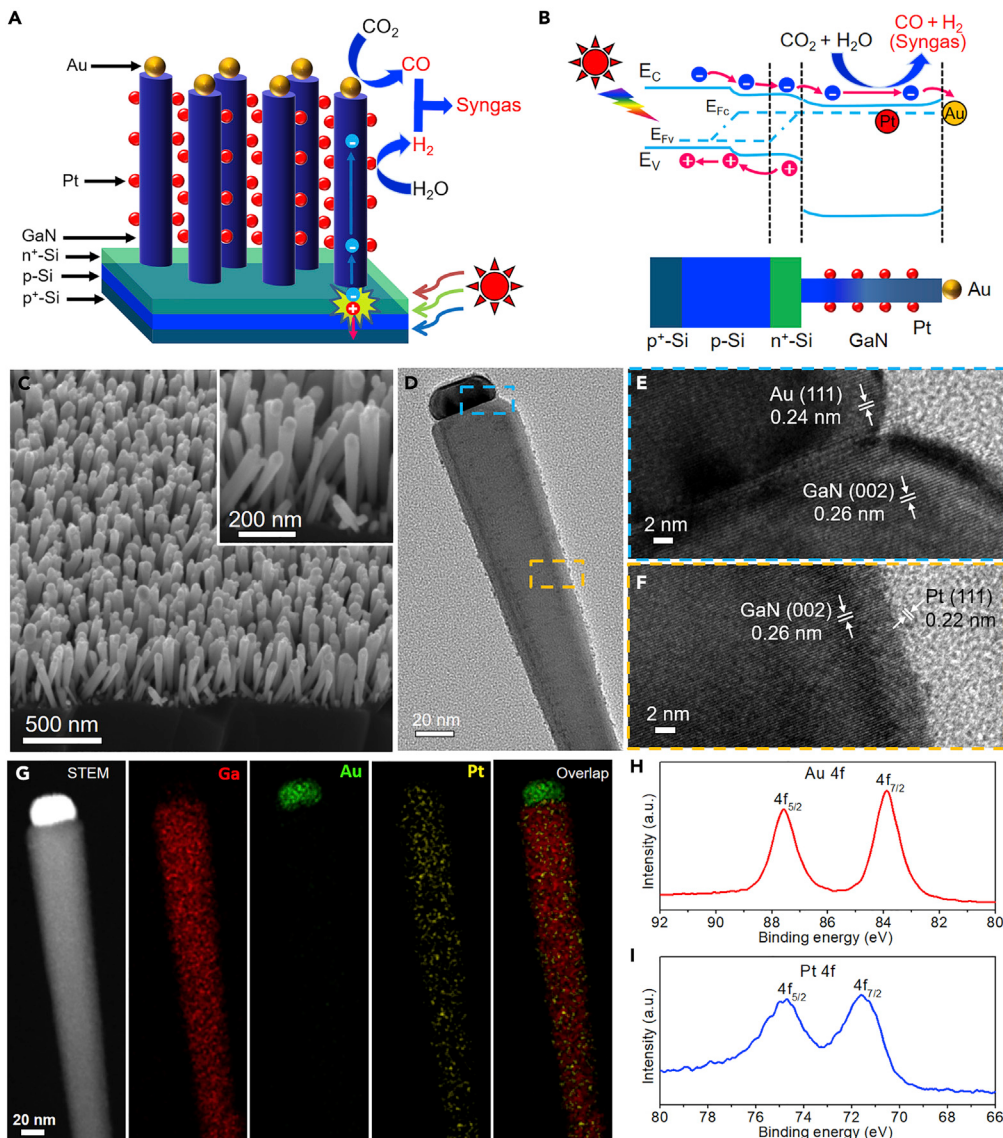
product can be controllably tuned in a wide range between 1:99 and 10:1 by simply varying the composition of dual cocatalysts. We also construct a bias-free solar syngas generation device in a tandem PEC cell with a solar-to-syngas (STS) efficiency of 0.63%.

RESULTS AND DISCUSSION

Theory-Guided Design of Enhanced Syngas Generation by a Decoupling Strategy

Density functional theory (DFT) studies were conducted first to gain insight into the design of high-performing catalyst for syngas generation from CO₂ reduction at an atomicistic level. CO₂RR to CO proceeds via reaction intermediates of $^{*}\text{COOH}$ and $^{*}\text{CO}$ that bind metal surfaces through a carbon atom (Figure 1A), whereas HER takes place via $^{*}\text{H}$ intermediate (Figure 1B). The binding energies of key reaction intermediates, $^{*}\text{COOH}$ and $^{*}\text{CO}$ in the CO₂RR to CO, and $^{*}\text{H}$ in HER, are reaction descriptors to determine the corresponding catalytic activity (Hansen et al., 2013; Bagger et al., 2017). In addition, two $^{*}\text{CO}$ protonation steps to form $^{*}\text{COH}$ and $^{*}\text{CHO}$ were also considered as they are possible potential-determining steps that compete with CO desorption step (Shi et al., 2014). The volcano plot can be obtained according to the Sabatier principle, since the optimal catalyst binds the reaction intermediates neither too strongly nor too weakly (Peterson and Nørskov, 2012; Liu et al., 2017). Figures 1C and 1D show the theoretical predicted volcano plots of CO₂RR and HER activity versus the binding energy of $^{*}\text{CO}$ for eight face-centered cubic (fcc) transition metals, including H₂-generating ones (Pt, Ir, Rh, Ni, Pd), CO-generating ones (Au, Ag), and hydrocarbon-generating one (Cu) (Hori, 2018). The uniformity of the fcc crystal structure allows us to perform a better comparison of catalytic activity among various metals. In addition, we consider both (111) and (211) facets to represent terrace and step sites, respectively. The detailed fitting data of scaling relations are available in Figures S1 and S2. The free energy corrections for adsorbed and non-adsorbed species are listed in Table S1.

Among the fcc metals screened, it is found that Au and Ag locate on the right of the *CO/CO equilibrium line (black vertical dashed line), indicating facile CO desorption due to the weak binding energy of *CO. However, both Au and Ag display a low HER activity with a limiting potential larger than 0.4 eV as their bindings with *H are too weak. In contrast, Pt and Ni locate very near the top of the HER volcano plot with optimal binding of the *H intermediate, but both locate on the left of the *CO/CO equilibrium line that favors further reduction of *CO to other downstream products owing to stronger bindings with *CO.

**Figure 2. Design and Characterization of Photoelectrocatalyst with Dual Cocatalysts**

(A and B) (A) Schematic and (B) energy band diagram of $\text{AuPt}_x/\text{GaN}/\text{n}^+\text{-p Si}$ photocathode (not drawn to scale), showing the generation of syngas under sunlight illumination.

(C–F) (C) 45°-tilted SEM, (D) TEM, (E) and (F) HRTEM images of $\text{AuPt}_{0.2}/\text{GaN}/\text{n}^+\text{-p Si}$ sample. The HRTEM images of (E) and (F) are obtained from the blue and yellow boxed areas in (D), respectively. See also Figure S4.

(G–I) (G) STEM-EDX elemental mapping images. XPS of (H) Au 4f and (I) Pt 4f.

The above findings demonstrate that it is challenging to develop efficient PEC syngas generation with optimal activity for both CO and H₂ evolution using a single monofunctional site, suggesting the necessity to decouple the two reactions using dual catalytic sites. As Au (Pt) is predicted to be more active for CO evolution (H₂ evolution) than that of Ag (Ni) in the DFT calculations, we selected Au and Pt as representative CO-generating and H₂-generating cocatalysts to demonstrate the decoupling strategy for enhanced PEC syngas generation.

Design and Characterization of Photoelectrocatalyst with Dual Cocatalysts

Experimentally, we integrated spatially separated dual cocatalysts of a Au CO-generating site and a Pt H₂-generating site with a material platform of GaN nanowire arrays on n⁺-p Si (abbreviated as $\text{AuPt}_x/\text{GaN}/\text{n}^+\text{-p Si}$, where x denotes the Pt/Au molar ratio). The schematic design and energy band diagram of $\text{AuPt}_x/\text{GaN}/\text{n}^+\text{-p Si}$

n^+ -p Si are illustrated in Figures 2A and 2B. The GaN/ n^+ -p Si platform takes advantage of the strong light-harvesting of Si (bandgap of 1.1 eV) and efficient electron extraction/transportation effect as well as large surface area provided by GaN nanowires (Vanka et al., 2018; Zhou et al., 2018). The nanowires allow high mass loadings of electrocatalyst and enhance the light absorption with decreased light reflection (Deng et al., 2019a). Significantly, the optical absorption and electrochemical reaction are decoupled spatially and functionally in the multi-dimensional structure, providing a unique platform to tune the product distribution by simply varying the cocatalyst composition. Under light illumination, the narrow bandgap of n^+ -p Si junction is readily photoexcited by the major portion of solar spectrum to generate electron-hole pairs for the reactions. The light absorption of GaN nanowires is negligible owing to its large bandgap of 3.4 eV. Because the conduction band edges of GaN and Si are closely aligned and both Si and GaN are heavily n-type doped, the photogenerated electrons can be readily migrated from Si to GaN (Vanka et al., 2018).

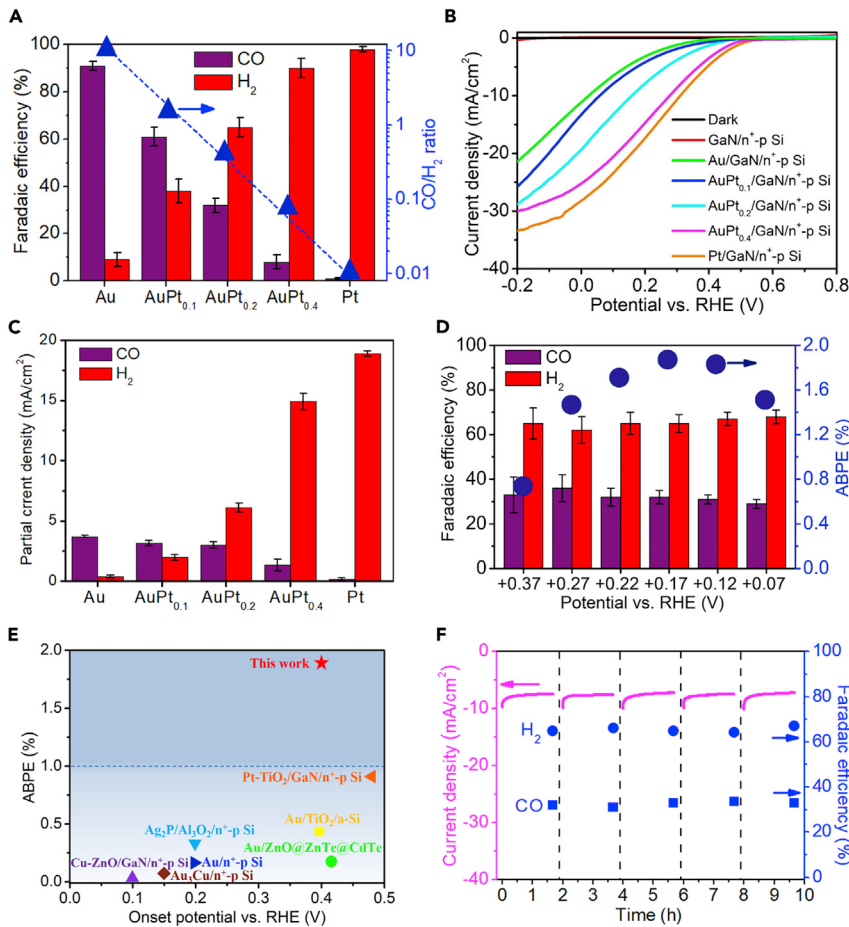
The sample was synthesized in two main steps. First, GaN nanowire arrays were grown on n^+ -p Si wafer by molecular beam epitaxy. Next, Au nanoparticles were decorated at the tip of GaN nanowires using e-beam evaporation followed with thermal annealing, and Pt nanoparticles were anchored on the side of GaN nanowires by photodeposition using H_2PtCl_6 as Pt precursor (see Methods and Figure S3 for synthesis and details). The spatial separation of dual cocatalysts, i.e., Au on the polar surface (top surface) and Pt on the nonpolar surface (side surface) of GaN nanowires, could controllably align the CO evolution rate and H_2 evolution rate in a balanced manner to achieve tunable syngas composition.

The morphology and chemical component of $AuPt_{0.2}/GaN/n^+$ -p Si sample were examined by scanning electron microscopy (SEM), transmission electron microscopy (TEM), X-ray diffraction (XRD), energy-dispersive X-ray spectroscopy (EDX) mapping, X-ray photoelectron spectroscopy (XPS), and inductively coupled plasma-atomic emission spectroscopy (ICP-AES) analysis. The cross-sectional SEM image (Figure 2C) indicates an average length of 350 nm and a diameter of 40 nm for the GaN nanowires and a size ranging from 20 to 40 nm for Au tips. TEM image (Figure 2D) indicates the Au-tipped structure and 1–2 nm Pt nanoparticles on the side surface of GaN nanowire. High-resolution (HR) TEM images in Figures 2E and 2F, and Figure S4 show the (111) facets of Au and Pt and (002) lattice plane of GaN, indicating the nanowire growth along the c-axis direction. XRD results confirmed the (111) plain of Au and (002) plane of GaN (Figure S5). The absence of XRD peaks of Pt nanoparticles is likely due to its low content and small crystalline size of 1–2 nm. The scanning transmission electron microscopy EDX (STEM-EDX) elemental mapping of a single nanowire (Figure 2G) confirmed the Au-tipped structure and Pt distributed uniformly on the lateral surface of nanowire. The XPS analysis in Figures 2H and 2I indicates metallic Au (Au^0) and Pt (Pt^0). ICP-AES analysis reveals the loading amounts of Au and Pt in $AuPt_{0.2}/GaN/n^+$ -p Si were 8.5 and 1.7 nmol cm^{-2} , respectively, with Au/Pt molar ratio of 5. By varying the introduced amount of Pt precursor, $AuPt_x/GaN/n^+$ -p Si samples with different cocatalyst ratios ($AuPt_{0.1}$, $AuPt_{0.2}$, $AuPt_{0.4}$) were prepared, with the loading amounts determined by ICP-AES analysis (Table S2). The TEM images of $AuPt_x/GaN/n^+$ -p Si with different cocatalyst compositions are shown in Figure S6, showing Au located at the tip and the well dispersion of Pt nanoparticles across the nanowire.

Realization of Efficient and Tunable PEC Syngas Generation

PEC studies of $AuPt_x/GaN/n^+$ -p Si photocathodes were investigated in CO_2 -saturated 0.5 M $KHCO_3$ solution (pH 7.5) under air mass 1.5 global (AM 1.5G) standard one-sun illumination (100 mW cm^{-2}) in a three-electrode configuration. Figure 3A shows the Faradaic efficiencies (FEs) for CO and H_2 on $AuPt_x/GaN/n^+$ -p Si photocathodes with different cocatalyst compositions at an applied potential of +0.17 V versus reversible hydrogen electrode (RHE). Hereafter, all the PEC potentials are reported with respect to the RHE unless otherwise specified. The corresponding chronoamperometry data are shown in Figure S7. Dominant CO evolution and H_2 evolution were detected on $Au/GaN/n^+$ -p Si and $Pt/GaN/n^+$ -p Si, respectively. With the increase of x from 0.1 to 0.4 in $AuPt_x/GaN/n^+$ -p Si, an increased FE for H_2 evolution with concurrently decreased FE for CO evolution was observed. By systematically tuning the cocatalyst composition, the ratio of CO/ H_2 could be tailored in a wide range from 1:99 to 10:1. In particular, $AuPt_{0.2}/GaN/n^+$ -p Si produced syngas with a CO/ H_2 ratio of 1:2, which is a desirable composition for methanol and hydrocarbon fuels synthesis (Foit et al., 2017). As for all the samples, a unity FE was obtained for the cogeneration of CO and H_2 , with no other gaseous or liquid products detected.

Figure 3B shows the current-potential ($J-V$) curves of different photocathodes. Compared with the negligible photocurrent density of bare GaN/n^+ -p Si, $Au/GaN/n^+$ -p Si displays a photocurrent density of 21

**Figure 3. Realization of Efficient and Tunable PEC Syngas Generation**

(A) FEs for CO (purple bars) and H₂ (red bars), and CO/H₂ ratio of AuPt_x/GaN/n⁺-p Si photocathodes at +0.17 V versus RHE.

(B) J-V curves.

(C) Partial current density for CO (purple bars) and H₂ (red bars) of AuPt_x/GaN/n⁺-p Si photocathodes at +0.17 V versus RHE.

(D) FEs for CO (purple bars) and H₂ (red bars), and ABPE of AuPt_{0.2}/GaN/n⁺-p Si as a function of applied potential.

(E) Performance comparison of AuPt_{0.2}/GaN/n⁺-p Si with state-of-the-art photocathodes for PEC CO₂ reduction into CO/syngas.

(F) Chronoamperometry data and FEs for CO and H₂ of AuPt_{0.2}/GaN/n⁺-p Si photocathode at +0.17 V versus RHE. The dashed lines indicate cleaning of photoelectrode with DI water and purging of PEC chamber with CO₂. Experimental conditions: CO₂-saturated 0.5 M KHCO₃ aqueous solution (pH 7.5), AM 1.5G one-sun illumination (100 mW cm⁻²). Error bars represent one standard deviation of multiple independent measurements.

mA cm⁻² at -0.2 V with an onset potential of ~0.4 V. With the incorporation of Pt, the onset potential shifts gradually to ~0.5 V, and the photocurrent increases owing to high activity of Pt for HER. The partial current densities of CO and H₂ at +0.17 V are shown in Figure 3C. With the increase of Pt content, the partial current density for H₂ increases, whereas CO was kept nearly unchanged with the increase of Pt/Au ratio up to 0.2, indicating the access of balanced and simultaneously high CO₂RR and HER activity in AuPt_{0.2}/GaN/n⁺-p Si sample.

It is worth noting that the spatial separation of CO evolution and H₂ evolution sites is critical to controllably tune syngas composition with a wide ratio of CO/H₂. A control experiment using Pt(NH₃)₄Cl₂ as Pt precursor obtained sample with Pt nanoparticles located on the polar surface of GaN nanowire in close proximity to Au (Figure S8). In contrast to the spatially separated dual cocatalysts, the mixture of cocatalysts produces a dominant H₂ evolution with FE over 90% and low controllability of syngas composition as a function of

cocatalyst composition (Figure S9). It is a highly competitive process between adjacent Pt and Au for electron transfer, which favors the HER on Pt owing to its kinetic feasibility. The different photodeposition behaviors using different Pt precursors are ascribed to the stronger adsorption of PtCl_6^{2-} anions on GaN surface than $\text{Pt}(\text{NH}_3)_4^{2+}$ cations (Figure S10). Pt nanoparticles were preferentially deposited on the sidewall of GaN nanowires using H_2PtCl_6 as Pt precursor owing to a sorption-determined deposition mechanism (Wenderich et al., 2014). In contrast, Pt was photodeposited on the tip of nanowire in close proximity with Au where electrons reside when using $\text{Pt}(\text{NH}_3)_4\text{Cl}_2$ as Pt precursor owing to negligible adsorption of $\text{Pt}(\text{NH}_3)_4^{2+}$ cations on nanowire (Li et al., 2013, 2020).

Figure 3D shows the FEs for CO and H_2 on $\text{AuPt}_{0.2}/\text{GaN/n}^+\text{-p Si}$ at an applied potential between +0.37 and +0.07 V. The CO/ H_2 ratio was kept at nearly 1:2 in the PEC potential range investigated. The ABPE at different applied potentials were calculated according to the measured photocurrent density and FEs for CO and H_2 (Equation 7, presented in *Transparent Methods*). The ABPE reached a maximum of 1.88% at +0.17 V, which is more than two times higher than that of state-of-the-art photocathodes (Figure 3E, and the details including the reference sources can be found in Table S3). The durability of $\text{AuPt}_{0.2}/\text{GaN/n}^+\text{-p Si}$ photocathode was also investigated, as shown in Figure 3F. Both the photocurrent density and product selectivity remain unchanged for a period of 10 h. In addition, the SEM, TEM, and XPS analysis of $\text{AuPt}_{0.2}/\text{GaN/n}^+\text{-p Si}$ sample after the PEC reaction show no change of GaN nanowires and Au-Pt cocatalysts (Figure S11). The turnover number for CO (TON_{CO}), defined as the ratio of the evolved CO amount (40 μmol) to the amount of Au catalyst (1.7 nmol, calculated from the catalyst loadings of 8.5 nmol cm^{-2} and electrode sample area of 0.2 cm^2), was calculated to be 23,500. However, this value is a low limit because the calculation is based on the 30 nm bulk Au catalyst instead of only the relevant surface sites. The surface atom ratio of Au NPs with 30 nm size was calculated to be ~5% using theoretical Au nanoparticle model. By considering only the surface sites, the TON_{CO} was calculated to be 470,000, which is the highest reported value to date for PEC CO/syngas production from CO_2RR to our knowledge (Chu et al., 2018; Rosser et al., 2016; Kumagai et al., 2017). In addition, the turnover frequency for CO (TOF_{CO}) was calculated to be 56,400 h^{-1} considering a duration time of 500 min. A comparison of TOF values was shown in Table S4, showing the TOF_{CO} value reported in this work is comparable with most of the state-of-the-art catalysts for (photo)electrochemical CO_2 reduction into CO. The mass activity of syngas production for $\text{AuPt}_{0.2}/\text{GaN/n}^+\text{-p Si}$ photocathode at +0.17 V was calculated ~4.7 A/mg, which is one or two orders of magnitude higher than the conventional planar Au-based CO/syngas generation system (Li et al., 2019; Feng et al., 2015; Sun et al., 2017). The large surface-to-volume ratio of GaN nanowire allows high-density catalytic sites with a significantly reduced loading amount compared with the planar structure.

To understand the role of GaN nanowires, control experiments using $\text{AuPt}_{0.2}/\text{n}^+\text{-p Si}$ planar sample in the absence of GaN nanowires were performed. The J-V curve of $\text{AuPt}_{0.2}/\text{n}^+\text{-p Si}$ planar sample displays a low photocurrent density (0.5 mA cm^{-2} at +0.17 V) and a poor onset potential of 0.25 V (Figure S12). Meanwhile, the FE for CO of $\text{AuPt}_{0.2}/\text{n}^+\text{-p Si}$ is 9% at +0.17 V, which is much lower than that of 32% for $\text{AuPt}_{0.2}/\text{GaN/n}^+\text{-p Si}$ (Figure S13). These results indicate the critical role of GaN nanowires as a superior structural scaffold to enhance the PEC performance. To demonstrate that the generated CO from CO_2 reduction, isotopic experiment using $^{13}\text{CO}_2$ was conducted. The signal at $m/z = 29$ assigned to ^{13}CO appeared in the gas chromatography-mass spectrometry analysis and no signal of ^{12}CO was detected (Figure S14). In addition, blank test performed in Ar-purged Na_2SO_4 aqueous solution showed no formation of CO, confirming the CO product originated from the reduction of CO_2 .

Demonstration of Unassisted Overall Syngas Generation in a Tandem PEC Cell

We constructed an unassisted overall solar CO_2 reduction device by pairing the $\text{AuPt}_{0.2}/\text{GaN/n}^+\text{-p Si}$ photocathode with a BiVO_4 -based photoanode to form a p/n tandem PEC cell. BiVO_4 photoanode was chosen owing to its demonstrated relatively high photocurrent with an early onset potential (0.2–0.3 V versus RHE) (Kim and Choi, 2014; Kuang et al., 2017; Luo et al., 2011). The configuration of the device is shown in Figure 4A. In this configuration, the photovoltage is the sum of the two parts, and the longer wavelength photons that are not absorbed by the front BiVO_4 absorber are transmitted and harvested by the bottom Si absorber. The maximum operating current density of the device was predicted to be 1.2 mA cm^{-2} by overlapping the J-V curves of photoanode and photocathode in a three-electrode cell (Figure S14). This nonzero operating point indicates the unassisted overall solar CO_2 reduction could occur, which was confirmed in a two-electrode cell. Figure 4B shows the time course of the photocurrent and FEs for CO and

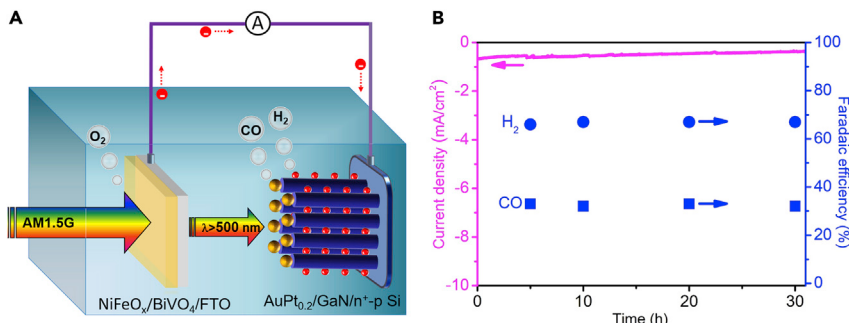


Figure 4. Demonstration of Unassisted Overall Syngas Generation in a Tandem PEC Cell

(A) Schematic illustration of the tandem cell, consisting of AuPt_{0.2}/GaN/n⁺-p Si as the photocathode and NiFeO_x/BiVO₄ as the photoanode without bias.

(B) Unassisted syngas generation in a two-electrode tandem cell under AM 1.5G one-sun illumination (100 mW cm⁻²).

H₂ generated by the tandem PEC cell over a period of ~30 h. A stable CO/H₂ ratio of 1:2 with an average photocurrent density of ~0.5 mA cm⁻² was attained under no applied bias, which corresponds to an STS efficiency of 0.63%. The efficiency is higher than recently reported values in a PEC cell without external bias (Li et al., 2019; Andrei et al., 2020). Although the efficiency is lower than that reported in photovoltaic-electrolysis (PV-E) system (Schreier et al., 2015a, 2017; Urbain et al., 2017; Zhang et al., 2019; Kim et al., 2019; Cheng et al., 2020), the PEC approach integrates the light harvesting and electrochemical process of PV-E process into a single and monolithic device via a direct semiconductor-electrolyte interface, providing potential advantages over the PV-E system in terms of cost and complexity. And it is expected that the STS efficiency of the PEC system could be enhanced further by employing better photoanode with higher photocurrent at the low bias region, which would improve the overlap of J-V curves between photocathode and photoanode.

Conclusion

In summary, we have demonstrated the decoupling of CO₂RR and HER using dual cocatalysts to overcome the efficiency bottleneck and composition uncontrollability of PEC syngas generation from aqueous CO₂. By spatially assembling a Au CO-generating cocatalyst and a Pt H₂-generating cocatalyst on the polar and nonpolar surfaces of GaN nanowires, respectively, a record ABPE of 1.88% was achieved on planar Si photocathode. In addition, the CO/H₂ ratio in the syngas mixture was controllably tuned in a wide range between 1:99 and 10:1 with a total unity Faradaic efficiency, by simply varying the composition of dual cocatalysts. And an STS efficiency of 0.63% without the application of an external bias was demonstrated in a tandem PEC cell as well. This work provides a promising route for the rational design of high-performance PEC syngas generation with controllable composition from aqueous CO₂ reduction.

Limitations of the Study

Although this study has demonstrated a decoupling strategy to enhance the syngas generation from photoelectrochemical CO₂ reduction, the overall syngas generation performance was largely limited by the CO evolution part, because CO₂RR requires a higher potential than the HER as shown in Figures 1C and 1D. The absolute HER activity was controlled by using rational amount of Pt to align with CO evolution rate for achieving meaningful syngas composition in this study. Further improvement of the syngas generation performance is expected if better catalyst for CO₂RR to CO is applied.

Resource Availability

Lead Contact

Further information and requests for resources and reagents should be directed to and will be fulfilled by the Lead Contact, Zetian Mi (ztmi@umich.edu).

Materials Availability

This study did not generate new unique reagents.

Data and Code Availability

This study did not generate/analyze datasets/code.

METHODS

All methods can be found in the accompanying [Transparent Methods supplemental file](#).

SUPPLEMENTAL INFORMATION

Supplemental Information can be found online at <https://doi.org/10.1016/j.isci.2020.101390>.

ACKNOWLEDGMENTS

The work was conducted at McGill University and the Michigan Center for Materials Characterization at the University of Michigan (NSF #DMR-0723032). We greatly acknowledge the financial support from Emissions Reduction Alberta (ERA), McGill Engineering Doctoral Award, and National Sciences and Engineering Research Council (NSERC) Discovery grant (grant # RGPIN-2017-05187). We also thank Supercomputer Consortium Laval UQAM McGill and Eastern Quebec for providing computing power and the National Natural Science Foundation of China for Excellent Young Scholar (51822604).

AUTHOR CONTRIBUTIONS

S.C., R.T.R., and P.G. prepared and characterized the sample and performed PEC test. P.O. performed DFT calculations. P.O. and J.S. analyzed calculation results. R.T.R., R.W., and H.N.T. conducted the nanowires growth. S.Z. and H.Z. contributed to result analysis and discussions. The manuscript was written by S.C. P.O., J.S., and Z.M. with contributions from other co-authors.

DECLARATION OF INTERESTS

The authors declare no competing interest.

Received: May 12, 2020

Revised: July 13, 2020

Accepted: July 15, 2020

Published: August 21, 2020

REFERENCES

- Andrei, V., Reuillard, B., and Reisner, E. (2020). Bias-free solar syngas production by integrating a molecular cobalt catalyst with perovskite-BiVO₄ tandems. *Nat. Mater.* 19, 189–194.
- Bagger, A., Ju, W., Varela, A.S., Strasser, P., and Rossmeisl, J. (2017). Electrochemical CO₂ reduction: a classification problem. *ChemPhysChem* 18, 3266–3273.
- Cheng, W.-H., Richter, M.H., Sullivan, I., Larson, D.M., Xiang, C., Brunschwig, B.S., and Atwater, H.A. (2020). CO₂ reduction to CO with 19% efficiency in a solar-driven gas diffusion electrode flow cell under outdoor solar illumination. *ACS Energy Lett.* 5, 470–476.
- Chu, S., Fan, S.Z., Wang, Y.J., Rossouw, D., Wang, Y.C., Botton, G.A., and Mi, Z. (2016). Tunable syngas production from CO₂ and H₂O in an aqueous photoelectrochemical cell. *Angew. Chem. Int. Ed.* 55, 14260–14264.
- Chu, S., Ou, P., Ghamari, P., Vanka, S., Zhou, B., Shih, I., Song, J., and Mi, Z. (2018). Photoelectrochemical CO₂ reduction into syngas with the metal/oxide interface. *J. Am. Chem. Soc.* 140, 7869–7877.
- Deng, J., Su, Y., Liu, D., Yang, P., Liu, B., and Liu, C. (2019a). Nanowire photoelectrochemistry. *Chem. Rev.* 119, 9221–9259.
- Deng, X., Li, R., Wu, S., Wang, L., Hu, J., Ma, J., Jiang, W., Zhang, N., Zheng, X., Gao, C., et al. (2019b). Metal-organic framework coating enhances the performance of Cu₂O in photoelectrochemical CO₂ reduction. *J. Am. Chem. Soc.* 141, 10924–10929.
- Feng, J.Y., Huang, H.T., Yan, S.C., Luo, W.J., Yu, T., Li, Z.S., and Zou, Z.G. (2020). Non-oxide semiconductors for artificial photosynthesis: progress on photoelectrochemical water splitting and carbon dioxide reduction. *Nano Today* 30, 100830.
- Feng, X., Jiang, K., Fan, S., and Kanan, M.W. (2015). Grain-boundary-dependent CO₂ electroreduction activity. *J. Am. Chem. Soc.* 137, 4606–4609.
- Foit, S.R., Vinke, I.C., de Haart, L.G.J., and Eichel, R.A. (2017). Power-to-syngas: an enabling technology for the transition of the energy system? *Angew. Chem. Int. Ed.* 56, 5402–5411.
- Hansen, H.A., Varley, J.B., Peterson, A.A., and Norskov, J.K. (2013). Understanding trends in the electrocatalytic activity of metals and enzymes for CO₂ reduction to CO. *J. Phys. Chem. Lett.* 4, 388–392.
- He, R., Zhang, A., Ding, Y., Kong, T., Xiao, Q., Li, H., Liu, Y., and Zeng, J. (2018). Achieving the widest range of syngas proportions at high current density over cadmium sulfoselenide nanorods in CO₂ electroreduction. *Adv. Mater.* 30, 1705872.
- Hori, Y. (2018). *Modern Aspects of Electrochemistry*, vol. 42 (Springer), pp. 89–189.
- Jang, J.-W., Cho, S., Magesh, G., Jang, Y.J., Kim, J.Y., Kim, W.Y., Seo, J.K., Kim, S., Lee, K.-H., and Lee, J.S. (2014). Aqueous-solution route to zinc telluride films for application to CO₂ reduction. *Angew. Chem. Int. Ed.* 53, 5852–5857.
- Jang, Y.J., Jang, J.W., Lee, J., Kim, J.H., Kumagai, H., Lee, J., Minegishi, T., Kubota, J., Domen, K., and Lee, J.S. (2015). Selective CO production by Au coupled ZnTe/ZnO in the photoelectrochemical CO₂ reduction system. *Energy Environ. Sci.* 8, 3597–3604.
- Kang, P., Chen, Z., Nayak, A., Zhang, S., and Meyer, T.J. (2014). Single catalyst electrocatalytic reduction of CO₂ in water to H₂+CO syngas mixtures with water oxidation to O₂. *Energy Environ. Sci.* 7, 4007–4012.

Kim, B., Seong, H., Song, J.T., Kwak, K., Song, H., Tan, Y.C., Park, G., Lee, D., and Oh, J. (2019). Over a 15.9% Solar-to-CO conversion from dilute CO₂ streams catalyzed by gold nanoclusters exhibiting a high CO₂ binding affinity. *ACS Energy Lett.* 5, 749–757.

Kim, T.W., and Choi, K.S. (2014). Nanoporous BiVO₄ photoanodes with dual-layer oxygen evolution catalysts for solar water splitting. *Science* 343, 990–994.

Kong, Q., Kim, D., Liu, C., Yu, Y., Su, Y., Li, Y., and Yang, P.D. (2016). Directed assembly of nanoparticle catalysts on nanowire photoelectrodes for photoelectrochemical CO₂ reduction. *Nano Lett.* 16, 5675–5680.

Kuang, Y.B., Jia, Q.X., Ma, G.J., Hisatomi, T., Minegishi, T., Nishiyama, H., Nakabayashi, M., Shibata, N., Yamada, T., Kudo, A., et al. (2017). Ultrastable low-bias water splitting photoanodes via photocorrosion inhibition and in situ catalyst regeneration. *Nat. Energy* 2, 16191.

Kumagai, H., Sahara, G., Maeda, K., Higashi, M., Abe, R., and Ishitani, O. (2017). Hybrid photocathode consisting of a CuGaO₂ p-type semiconductor and a Ru(II)-Re(II) supramolecular photocatalyst: non-biased visible-light-driven CO₂ reduction with water oxidation. *Chem. Sci.* 8, 4242–4249.

Landers, A.T., Fields, M., Torelli, D.A., Xiao, J., Hellstern, T.R., Francis, S.A., Tsai, C., Kibsgaard, J., Lewis, N.S., Chan, K., et al. (2018). The predominance of hydrogen evolution on transition metal sulfides and phosphides under CO₂ reduction conditions: an experimental and theoretical study. *ACS Energy Lett.* 3, 1450–1457.

Lee, J.H., Kattel, S., Jiang, Z., Xie, Z., Yao, S., Tackett, B.M., Xu, W., Marinkovic, N.S., and Chen, J.G. (2019). Tuning the activity and selectivity of electroreduction of CO₂ to synthesis gas using bimetallic catalysts. *Nat. Commun.* 10, 3724.

Li, C.C., Wang, T., Liu, B., Chen, M.X., Li, A., Zhang, G., Du, M.Y., Wang, H., Liu, S.F., and Gong, J.L. (2019). Photoelectrochemical CO₂ reduction to adjustable syngas on grain-boundary-mediated a-Si/TiO₂/Au photocathodes with low onset potentials. *Energy Environ. Sci.* 12, 923–928.

Li, R., Zhang, F., Wang, D., Yang, J., Li, M., Zhu, J., Zhou, X., Han, H., and Li, C. (2013). Spatial separation of photogenerated electrons and holes among {010} and {110} crystal facets of BiVO₄. *Nat. Commun.* 4, 1432.

Li, Z., Zhang, L., Liu, Y., Shao, C., Gao, Y., Fan, F., Wang, J., Li, J., Yan, J., Li, R., and Li, C. (2020). Surface polarity-induced spatial charge separation boosting photocatalytic overall water splitting on GaN nanorod arrays. *Angew. Chem. Int. Ed.* 59, 935–942.

Liu, X., Xiao, J., Peng, H., Hong, X., Chan, K., and Norskov, J.K. (2017). Understanding trends in

electrochemical carbon dioxide reduction rates. *Nat. Commun.* 8, 15438.

Luo, W.J., Yang, Z.S., Li, Z.S., Zhang, J.Y., Liu, J.G., Zhao, Z.Y., Wang, Z.Q., Yan, S.C., Yu, T., and Zou, Z.G. (2011). Solar hydrogen generation from seawater with a modified BiVO₄ photoanode. *Energy Environ. Sci.* 4, 4046–4051.

Peterson, A.A., and Nørskov, J.K. (2012). Activity descriptors for CO₂ electroreduction to methane on transition-metal catalysts. *J. Phys. Chem. Lett.* 3, 251–258.

Qiu, J., Zeng, G.T., Ha, M.A., Ge, M.Y., Lin, Y.J., Hettick, M., Hou, B.Y., Alexandrova, A.N., Javey, A., and Cronin, S.B. (2015). Artificial photosynthesis on TiO₂-passivated InP nanopillars. *Nano Lett.* 15, 6177–6181.

Ross, M.B., Li, Y., De Luna, P., Kim, D., Sargent, E.H., and Yang, P.D. (2019). Electrocatalytic rate alignment enhances syngas generation. *Joule* 3, 1–8.

Rosser, T.E., Windle, C.D., and Reisner, E. (2016). Electrocatalytic and solar-driven CO₂ reduction to CO with a molecular manganese catalyst immobilized on mesoporous TiO₂. *Angew. Chem. Int. Ed.* 55, 7388–7392.

Schreier, M., Curvat, L., Giordano, F., Steier, L., Abate, A., Zakeeruddin, S.M., Luo, J., Mayer, M.T., and Grätzel, M. (2015a). Efficient photosynthesis of carbon monoxide from CO₂ using perovskite photovoltaics. *Nat. Commun.* 6, 7326.

Schreier, M., Gao, P., Mayer, M.T., Luo, J.S., Moehl, T., Nazeeruddin, M.R., Tilley, S.D., and Grätzel, M. (2015b). Efficient and selective carbon dioxide reduction on low cost protected Cu₂O photocathodes using a molecular catalyst. *Energy Environ. Sci.* 8, 855–861.

Schreier, M., Héroguel, F., Steier, L., Ahmad, S., Luterbacher, J.S., Mayer, M.T., Luo, J., and Grätzel, M. (2017). Solar conversion of CO₂ to CO using earth-abundant electrocatalysts prepared by atomic layer modification of CuO. *Nat. Energy* 2, 17087.

Shan, B., Vanka, S., Li, T., Trojan-Gautier, L., Brenneman, M.K., Mi, Z., and Meyer, T.J. (2019). Binary molecular-semiconductor p-n junctions for photoelectrocatalytic CO₂ reduction. *Nat. Energy* 4, 290–299.

Sheng, W., Kattel, S., Yao, S., Yan, B., Liang, Z., Hawkhurst, C.J., Wu, Q., and Chen, J.G. (2017). Electrochemical reduction of CO₂ to synthesis gas with controlled CO/H₂ ratios. *Energy Environ. Sci.* 10, 1180.

Shi, C., Hansen, H.A., Lausche, A.C., and Norskov, J.K. (2014). Trends in electrochemical CO₂ reduction activity for open and close-packed metal surfaces. *Phys. Chem. Chem. Phys.* 16, 4720–4727.

Song, J.T., Ryoo, H., Cho, M., Kim, J., Kim, J.G., Chung, S.Y., and Oh, J. (2017). Nanoporous Au thin films on Si photoelectrodes for selective and efficient photoelectrochemical CO₂ reduction. *Adv. Energy Mater.* 7, 1601103.

Sun, K., Cheng, T., Wu, L., Hu, Y., Zhou, J., MacLennan, A., Jiang, Z., Gao, Y., Goddard, W.A., 3rd, and Wang, Z. (2017). Ultrahigh mass activity for carbon dioxide reduction enabled by gold-iron core-shell nanoparticles. *J. Am. Chem. Soc.* 139, 15608–15611.

Urbain, F., Tang, P., Carretero, N.M., Andreu, T., Gerling, L.G., Voz, C., Arbiol, J., and Morante, J.R. (2017). A prototype reactor for highly selective solar-driven CO₂ reduction to synthesis gas using nanosized earth-abundant catalysts and silicon photovoltaics. *Energy Environ. Sci.* 10, 2256–2266.

Vanka, S., Arca, E., Cheng, S., Sun, K., Botton, G.A., Teeter, G., and Mi, Z. (2018). High efficiency Si photocathode protected by multifunctional GaN nanostructures. *Nano Lett.* 18, 6530–6537.

Wenderich, K., Klaassen, A., Siretanu, I., Mugele, F., and Mul, G. (2014). Sorption-determined deposition of platinum on well-defined platelike WO₃. *Angew. Chem. Int. Ed.* 53, 12476–12479.

White, J.L., Baruch, M.F., Pander, J.E., III, Hu, Y., Fortmeyer, I.C., Park, J.E., Zhang, T., Liao, K., Gu, J., Yan, Y., et al. (2015). Light-driven heterogeneous reduction of carbon dioxide: photocatalysts and photoelectrodes. *Chem. Rev.* 115, 1288–12935.

Zhang, H., Ming, J., Zhao, J., Gu, Q., Xu, C., Ding, Z., Yuan, R., Zhang, Z., Lin, H., Wang, X., et al. (2019). High-Rate, Tunable syngas production with artificial photosynthetic cells. *Angew. Chem. Int. Ed.* 58, 7718–7722.

Zhang, L., Zhao, Z.J., Wang, T., and Gong, J. (2018). Nano-designed semiconductors for electro- and photoelectro-catalytic conversion of carbon dioxide. *Chem. Soc. Rev.* 47, 5423–5443.

Zhang, Y.-J., Sethuraman, V., Michalsky, R., and Peterson, A.A. (2014). Competition between CO₂ reduction and H₂ evolution on transition-metal electrocatalysts. *ACS Catal.* 4, 3742–3748.

Zhou, B., Kong, X., Vanka, S., Chu, S., Ghamari, P., Wang, Y., Pant, N., Shih, I., Guo, H., and Mi, Z. (2018). Gallium nitride nanowire as a linker of molybdenum sulfides and silicon for photoelectrocatalytic water splitting. *Nat. Commun.* 9, 3856.

Zhou, B., Ou, P., Pant, N., Cheng, S., Vanka, S., Chu, S., Rashid, R.T., Botton, G., Song, J., and Mi, Z. (2020). Highly efficient binary copper-iron catalyst for photoelectrochemical carbon dioxide reduction toward methane. *Proc. Natl. Acad. Sci. U.S.A.* 117, 1330–1338.

Supplemental Information

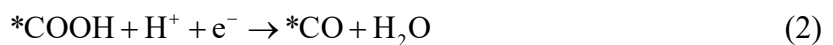
Decoupling Strategy for Enhanced Syngas Generation from Photoelectrochemical CO₂ Reduction

Sheng Chu, Pengfei Ou, Roksana Tonny Rashid, Pegah Ghamari, Renjie Wang, Hong Nhung Tran, Songrui Zhao, Huiyan Zhang, Jun Song, and Zetian Mi

Transparent Methods

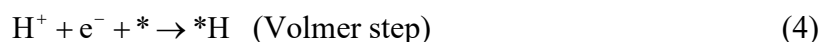
Density functional theory (DFT) calculations: DFT calculations were performed with BEEF-vdW (Wellendorff et al., 2012) exchange-correlation functional and projector augmented wave (PAW) pseudopotential (Blöchl, 1994; Kresse and Joubert, 1999) within the Vienna Ab-initio Simulation Package (VASP) (Kresse and Hafner, 1994; Kresse and Furthmüller, 1996). A cut-off energy of 400 eV was chosen, and structural optimization were achieved until the residual force on each atom was smaller than 0.01 eV Å⁻¹. A (3 × 3) and (3 × 1) surface unit with a four-layer slab were modeled for the (111) and (211) facets of fcc metals respectively, both containing 9 surface metal atoms per supercell. All slabs were spaced more than 20 Å perpendicular to the slab surface to avoid interaction due to their periodicity. A 4 × 4 × 1 Monkhorst-Pack mesh of k-points (Monkhorst and Pack, 1976) was used both for (111) and (211) facets. When relaxing the geometries, adsorbates and the top two layers were allowed to relax, while the bottom two layers were fixed to their initial bulk positions.

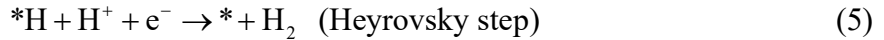
The reaction mechanism of CO₂ reduction to CO in an aqueous solution is suggested to include the following steps (Sheng et al., 2017):



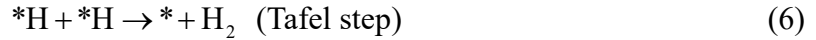
where * denotes either a surface-bound species or a vacant catalytic active site.

The HER consists of two consecutive proton-electron pair transfer steps:





or



Free energy corrections for adsorbates and gas molecules: The CO₂RR and HER activity maps were calculated by computational hydrogen electrode (CHE) model suggested by Nørskov et al (Nørskov et al., 2004). By employing the CHE model, a proton/electron ($\text{H}^+ + \text{e}^-$) in solution can be directly treated and the effect of a bias can be applied by shifting by ΔG by $+neU$, where n is the number of proton-electron pairs transferred, e is the elementary positive charge, and U is the applied potential. The free energy change (ΔG) is calculated as $\Delta G = \Delta E + \Delta ZPE + \int C_p dT - T\Delta S$, where ΔE is the total energy directly obtained from DFT calculations, ΔZPE is the change in zero-point energy, C_p is the heat capacity, T is temperature, and ΔS is the change in entropy. The temperature is set to 298.15 K to compare current DFT results with the experimental data. The contributions to the free energy for each adsorbate involved in the lowest-energy pathways are listed in Table S1. As indicated in a previous study (Tripković et al., 2010), the reaction intermediates would be stabilized by the hexagonal water overlayer above them, therefore the solvation correction was also employed by applying a $^*\text{COOH}$ and $^*\text{CO}$ stabilization of 0.25 and 0.1 eV, respectively.

DFT calculations of non-adsorbed species were performed using the same techniques as described above for adsorbed species, except with a Fermi-level smearing of 0.01 eV. The components of the energy calculations for all non-adsorbed species are also listed in Table S1.

Sample synthesis: GaN nanowire arrays were grown on planar p-n Si wafer by plasma-assisted molecular beam epitaxy as previously described (Vanka et al., 2018). Au nanoparticles were deposited on GaN nanowires using an e-beam evaporator at a deposition rate of 0.1 Å/s for 500 s, followed with thermal annealing in Ar at 650 °C for 2 min. During the annealing process, small Au nanoparticles migrated and coalesced to form large Au nanoparticles on GaN nanowires for decreasing the surface energy (Sui et al., 2013). Au was favourable to grow on the *c*-plane of GaN nanowires as a tipped heterostructure. This can be explained by the smaller formation energy for Au on *c*-plane GaN, partly due to the smaller lattice mismatch between Au(111) and *c*-plane GaN compared to *m*-plane GaN (0.24, 0.26 and 0.28 nm, respectively) (Li et al., 2014). Prior to the Au e-beam deposition, the GaN nanowires on p-n Si substrate was pre-treated with concentrated HCl solution for 30 s to remove native oxide. Pt nanoparticles were deposited on GaN nanowires by photodeposition using H₂PtCl₆ (99.9%, Sigma Aldrich) as precursor from an aqueous methanol solution (15 mL methanol and 60 mL deionized water). 2, 5 and 12 μL of 0.2 M H₂PtCl₆ were used for the preparation of AuPt_{0.1}/GaN/n⁺-p Si, AuPt_{0.2}/GaN/n⁺-p Si and AuPt_{0.4}/GaN/n⁺-p Si, respectivily. NiFeO_x/BiVO₄ photoanode was prepared according to a previously reported method (Kim and Choi, 2014; Kobayashi et al., 2018).

Characterization: ICP-AES analyses were performed on a Thermo Scientific iCAP 6000 Series inductively coupled plasma–atomic emission spectroscopy instrument to determine the loading amount of metal cocatalysts. The samples were digested in aqua regia (HNO₃:HCl=1:3) at 95 °C for 3 h before the analysis. The morphology of samples was characterized by SEM and TEM. SEM images were acquired from an Inspect F-50 FE-SEM system at an accelerating

voltage of 5 keV. TEM images were attained on FEI Tecnai G2 F20 microscope at 200 keV, with EDX attached. The nanowires were scratched off from the Si substrate onto a Cu TEM grid. Surface chemical compositions of samples were analyzed by XPS in a Thermo Scientific K-Alpha XPS system with a monochromatic Al $K\alpha$ source ($h\nu = 1486.6$ eV). The binding energies were calibrated using the C1s peak at 284.8 eV as the reference.

PEC measurements: PEC CO₂ reduction was performed in a three-electrode configuration with AuPt_x/GaN/n⁺-p Si as the working electrode, Pt wire as the counter electrode and Ag/AgCl as the reference electrode. The gastight PEC reactor has three compartments, including working compartment, reference compartment, and counter compartment. The compartments were separated by proton exchange membranes. Prior to PEC CO₂ reduction experiments, 40 mL electrolyte of 0.5 M KHCO₃ was added into the cell and purged with CO₂ for 30 min, resulting in electrolyte pH at 7.5. The light source was a solar simulator (Newport Oriel LCS-100) with a calibrated light intensity of 100 mW cm⁻² (1 sun) on the sample surface. The PEC data were collected by a potentiostat (Gamry Instruments, Interface 1000). The *J-V* curve was obtained at a scan rate of 20 mV/s. Chronoamperometry for product analysis was performed at a certain potential for 100 min. Gas products after the photoelectrolysis were analysed by a gas chromatograph (Shimadzu GC-8A) with a thermal conductivity detector for H₂ concentration, and a gas chromatograph (Shimadzu GC-2014) with a flame ionization detector for CO and hydrocarbons concentration. Each measurement was performed several times to check the consistency of experiments. The average values out of the multiple measurements were presented and error bars denote one standard deviation.

The applied bias photon-to-current efficiency (ABPE) was calculated using the following equation:

$$\text{ABPE}(\%) = \left[\frac{J(\text{mA}\cdot\text{cm}^{-2}) \times \text{FE}_{\text{CO}}(\%) \times (1.34 - V_{\text{bias}})(V) + J(\text{mA}\cdot\text{cm}^{-2}) \times \text{FE}_{\text{H}_2}(\%) \times (1.23 - V_{\text{bias}})(V)}{P_{\text{in}}(\text{mW}\cdot\text{cm}^{-2})} \right] \quad (7)$$

where J is the photocurrent density, FE_{CO} and FE_{H_2} are faradaic efficiency to produce CO and H₂ respectively, V_{bias} is the applied potential versus an ideal counter electrode for O₂ evolution (+1.23 V vs. RHE), and P_{in} is the light intensity (100 mW cm⁻²).

The unassisted overall solar-to-syngas (STS) efficiency η_{STS} was calculated using the following equation:

$$\eta_{\text{STS}}(\%) = \left[\frac{J(\text{mA}\cdot\text{cm}^{-2}) \times \text{FE}_{\text{CO}}(\%) \times 1.34(V) + J(\text{mA}\cdot\text{cm}^{-2}) \times \text{FE}_{\text{H}_2}(\%) \times 1.23(V)}{P_{\text{in}}(\text{mW}\cdot\text{cm}^{-2})} \right] \quad (8)$$

where J is the unbiased photocurrent density measured in a two-electrode cell.

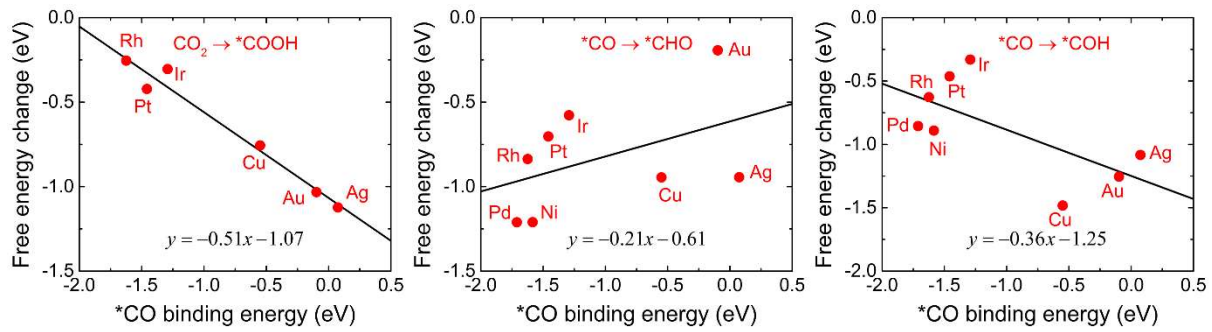


Figure S1. Scaling relations between the *CO binding energy and basic reactions in CO_2RR on transition metal fcc(111) facet. The fitted equations are shown in the insets. Related to Figure 1.

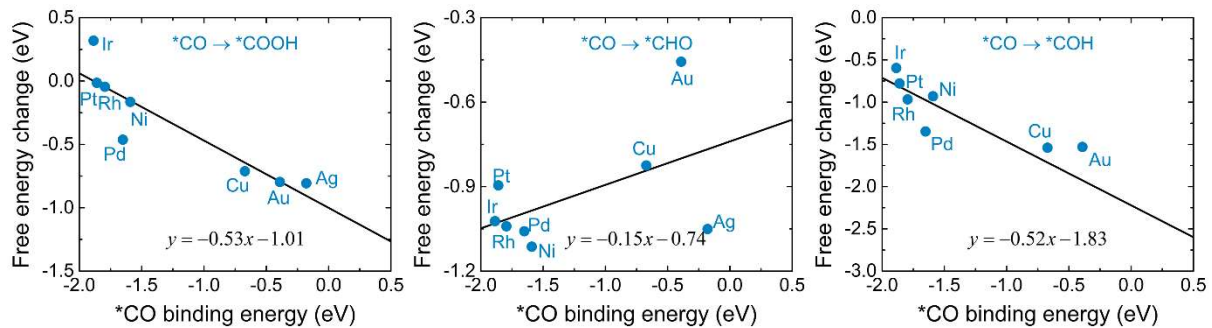


Figure S2. Scaling relations between the *CO binding energy and basic reactions in CO₂RR on transition metal fcc(211) facet. The fitted equations are shown in the insets. Related to Figure 1.

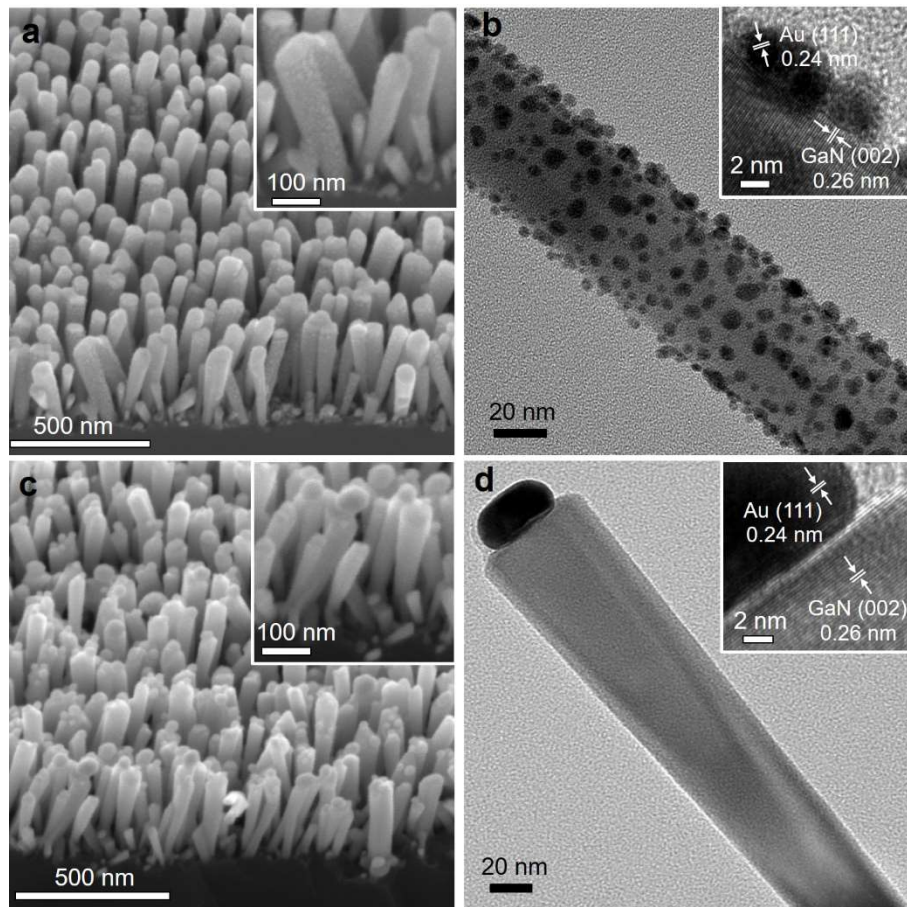


Figure S3. SEM and TEM images of Au/GaN/n⁺-p Si before (a, b) and after (c, d) annealing process. Related to Figure 2.

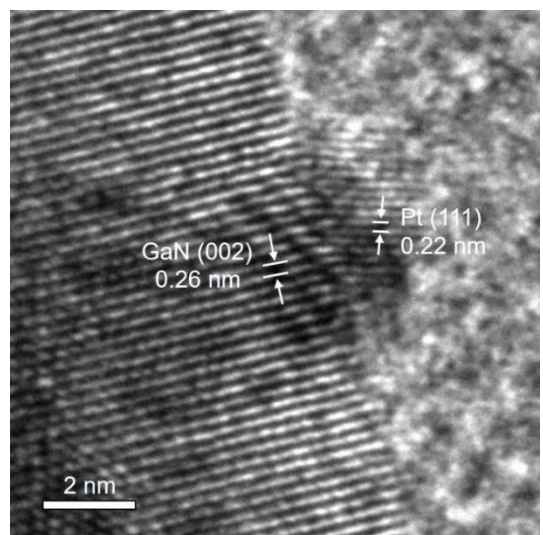


Figure S4. High-resolution TEM image of Pt nanoparticle on GaN nanowire. Related to Figure 2.

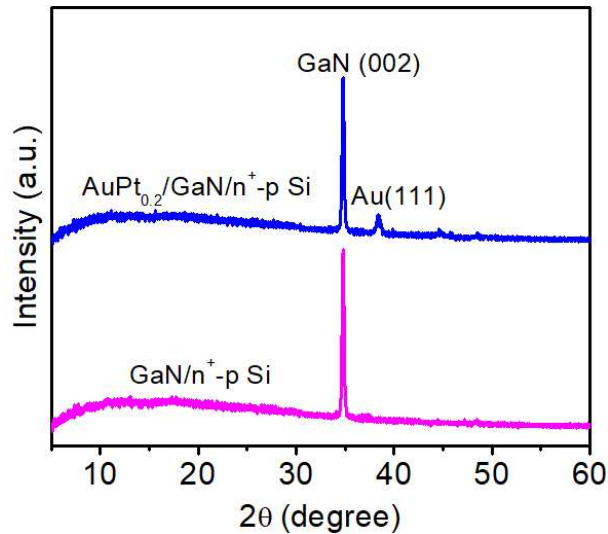


Figure S5. XRD patterns of $\text{GaN}/n^+ \text{-p Si}$ and $\text{AuPt}_{0.2}/\text{GaN}/n^+ \text{-p Si}$. Related to Figure 2.

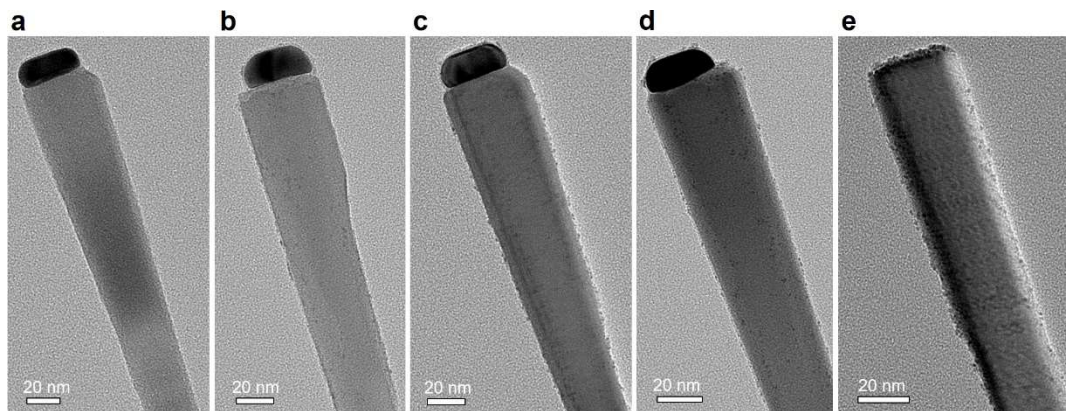


Figure S6. TEM images of (a) Au/GaN/n⁺-p Si, (b) AuPt_{0.1}/GaN/n⁺-p Si, (c) AuPt_{0.2}/GaN/n⁺-p Si, (d) AuPt_{0.4}/GaN/n⁺-p Si and (e) Pt/GaN/n⁺-p Si. Related to Figure 2.

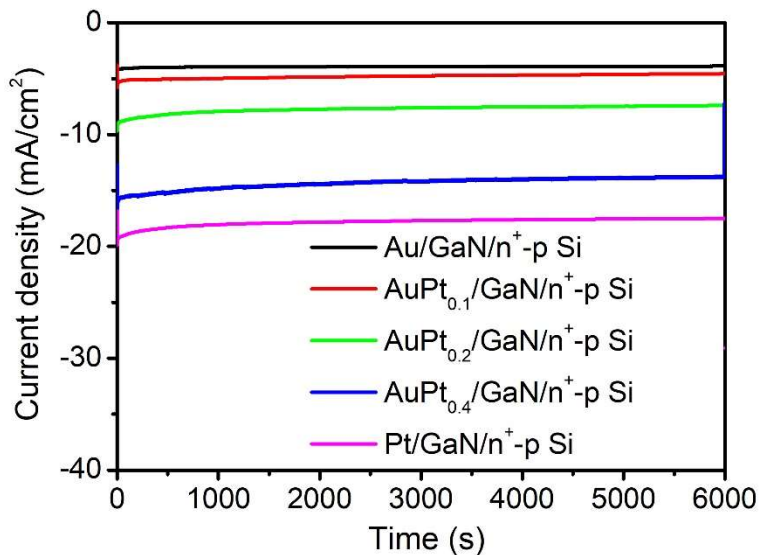


Figure S7. Chronoamperometry data of AuPt_x/GaN/n⁺-p Si photocathodes at +0.17 V vs RHE in CO₂-saturated 0.5 M KHCO₃ (pH 7.5) under AM 1.5G one-sun illumination. Related to Figure 3.

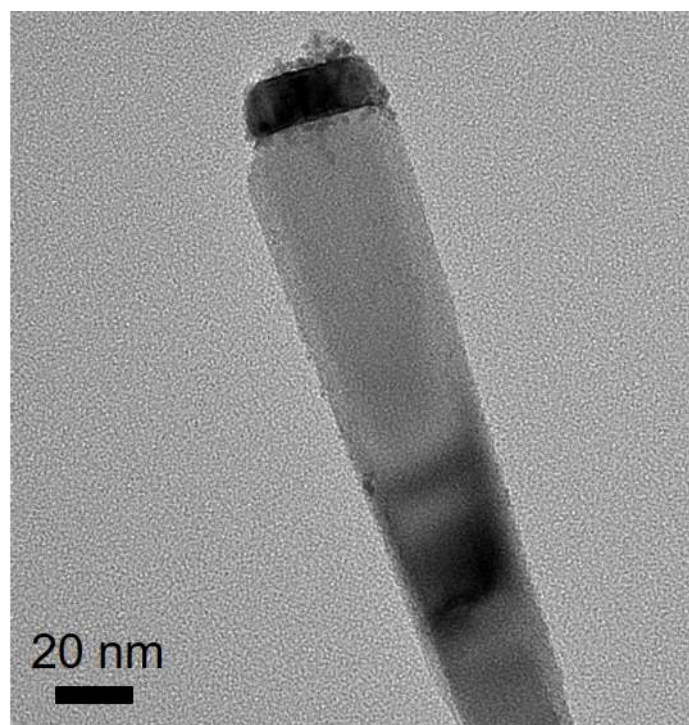


Figure S8. TEM image of $\text{AuPt}_{0.1}/\text{GaN}/n^+ \text{-} p$ Si using $\text{Pt}(\text{NH}_3)_4\text{Cl}_2$ as Pt precursor. Related to Figure 3.

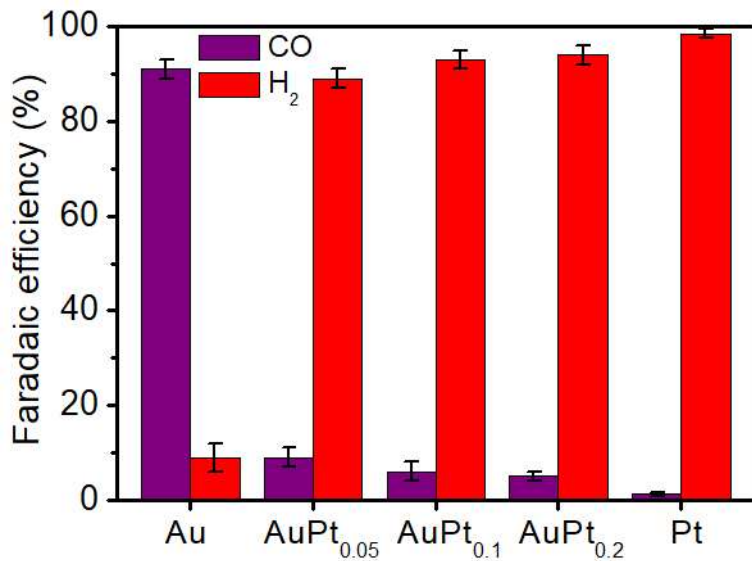


Figure S9. FEs for CO (purple bars) and H₂ (red bars) of AuPt_x/GaN/n⁺-p Si with different cocatalyst compositions at +0.17 V vs RHE using Pt(NH₃)₄Cl₂ as Pt precursor. Error bars represent one standard deviation of multiple independent measurements. Related to Figure 3.

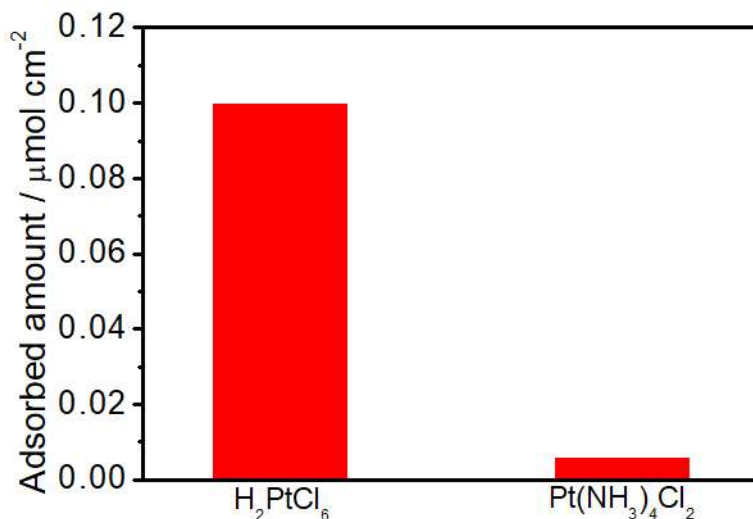


Figure S10. The adsorption amount of Pt precursor on Au/GaN/n⁺-p Si sample. 3 cm² of wafer sample was immersed in 50 mL H₂PtCl₆ or Pt(NH₃)₄Cl₂ aqueous solution (0.01 mmol/L) overnight. The Pt concentration in the solution was analyzed by ICP-AES, and the adsorbed Pt amount was calculated. The results show the stronger adsorption of PtCl₆²⁻ than that of Pt(NH₃)₄²⁺. Related to Figure 3.

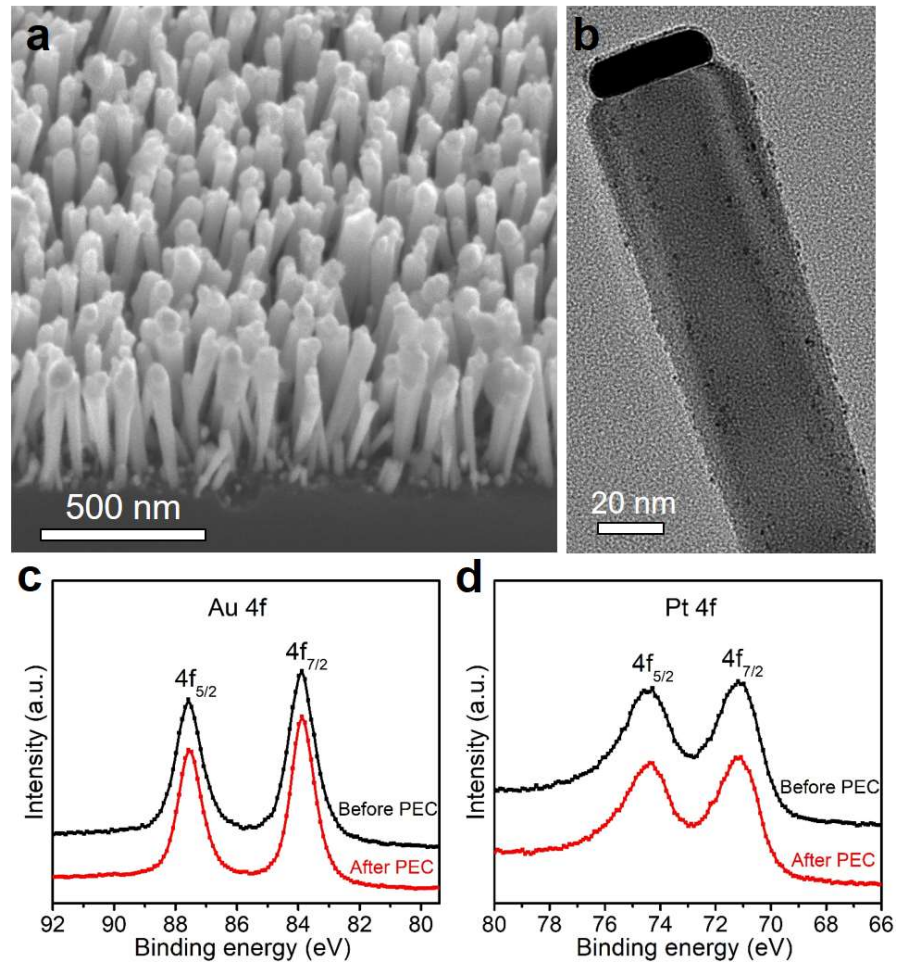


Figure S11. (a) SEM and (b) TEM images of $\text{AuPt}_{0.2}/\text{GaN}/n^+ \text{-} p$ Si photocathode after PEC stability test. XPS analysis of (c) Au 4f and (d) Pt 4f of $\text{AuPt}_{0.2}/\text{GaN}/n^+ \text{-} p$ Si photocathode before and after PEC stability test. Related to Figure 3.

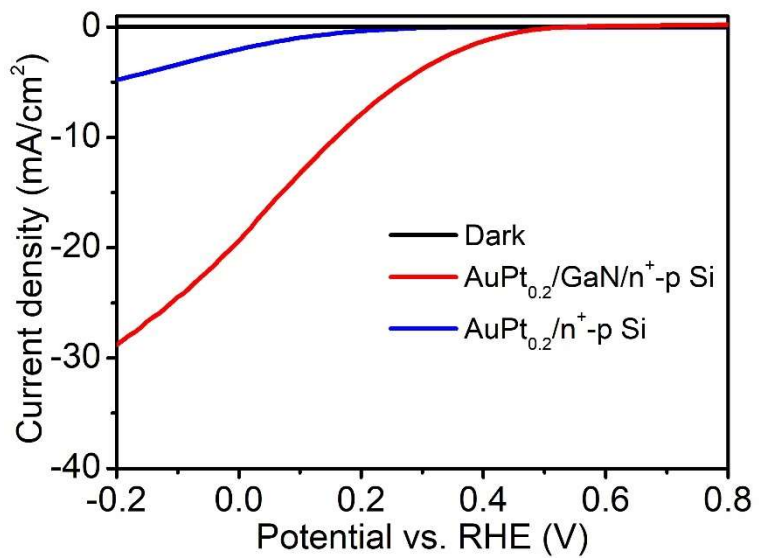


Figure S12. J - V curves of $\text{AuPt}_{0.2}/\text{n}^+ \text{-p Si}$ and $\text{AuPt}_{0.2}/\text{GaN}/\text{n}^+ \text{-p Si}$. Related to Figure 3.

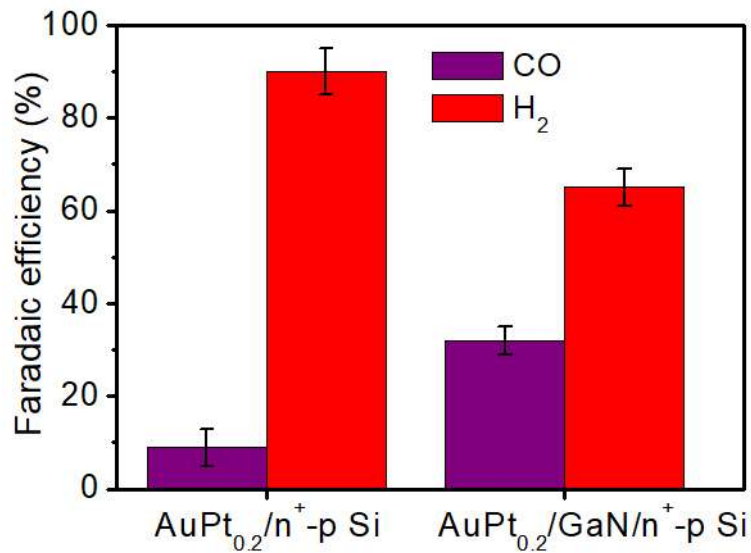


Figure S13. FEs for CO (purple bars) and H₂ (red bars) of AuPt_{0.2}/n⁺-p Si and AuPt_{0.2}/GaN/n⁺-p Si at +0.17 V vs RHE. The low FE for CO on AuPt_{0.2}/n⁺-p Si might be ascribed to the close proximity of Au and Pt cocatalysts when they deposited on planar Si substrate. Error bars represent one standard deviation of multiple independent measurements. Related to Figure 3.

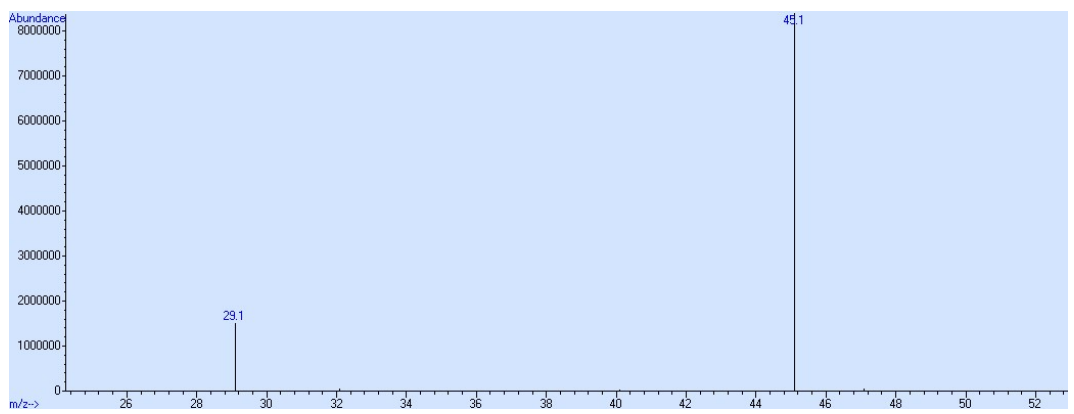


Figure S14. Mass spectrometry chromatogram of the gas phase analysis after ^{13}C -labeled isotope experiment. Related to Figure 3.

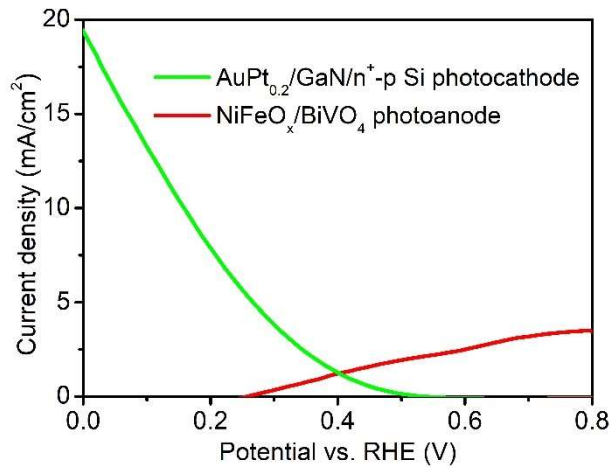


Figure S15. *J-V* curves for AuPt_{0.2}/GaN/n⁺-p Si (in CO₂-saturated 0.5 M KHCO₃ aqueous solution) and NiFeO_x/BiVO₄ photoanode (in 0.5 M KBi) in a three-electrode configuration. The photocathode data was plotted with the sign of the photocurrent inverted. Related to Figure 4.

Table S1 Contributions to the adsorbate free energy from the corrections of zero-point energy, heat capacity, and entropy, respectively. The assumed fugacity for each non-adsorbed species are also included. H₂ (ref) is used for the computational hydrogen electrode model as described in Computational Methods Section. Related to Figure 1.

Species	Fugacity (Pa)	ZPE (eV)	$\int C_p dT$ (eV)	-TS (eV)
*COOH	-	0.62	0.10	-0.27
*CO	-	0.19	0.08	-0.16
*H	-	0.16	0.01	-0.01
H ₂ (ref)	101325	0.27	0.09	-0.42
CO	101325	0.14	0.09	-0.67
H ₂ O	3534	0.58	0.10	-0.65
CO ₂	101325	0.31	0.10	-0.65

Table S2. ICP-AES analysis of Au and Pt loading amounts of different samples. Related to Figure 2.

Sample	Au/GaN/ n ⁺ -p Si	AuPt _{0.1} /GaN/ n ⁺ -p Si	AuPt _{0.2} /GaN/ n ⁺ -p Si	AuPt _{0.4} /GaN/ n ⁺ -p Si	Pt/GaN/ n ⁺ -p Si
Au (nmol cm ⁻²)	8.5	8.8	8.5	8.6	-
Pt (nmol cm ⁻²)	-	0.9	1.7	3.4	3.7

Table S3. Performance comparison of photocathodes for PEC CO₂ reduction into CO/syngas at underpotential (more positive than the equilibrium potential $E^\circ(\text{CO}_2/\text{CO}) = -0.11 \text{ V vs RHE}$). Related to Figure 3.

Photocathode	Light intensity (mW cm ⁻²)	Onset potential (V vs RHE) ^[a]	FE _{CO} (%) ^[b]	ABPE (%) ^[c]	Refs
Cu-ZnO/GaN/n ⁺ -p Si	800	0.1	70	~0.01	Chu et al., 2016
Au ₃ Cu/n ⁺ -p Si	20	0.15	80	0.07	Kong et al., 2016
Au/n ⁺ -p Si	100	0.2	91	0.12	Song et al., 2017
Au/ZnO@ZnTe@CdTe	100	0.45	67	0.18	Jang et al., 2016
Ag ₂ P/Al ₂ O ₃ /n ⁺ -p Si	100	0.3	67	0.3	Li et al., 2019
Au/TiO ₂ /a-Si	100	0.4	50	0.42	Li et al., 2019
Pt-TiO ₂ /GaN/n ⁺ -p Si	800	0.5	78	0.87	Chu et al., 2018
Cu ₃ (BTC) ₂ /Cu ₂ O	100	-1.77 V vs Fe/Fe ⁺	95	0.83	Deng et al., 2019
AuPt/GaN/n⁺-p Si	100	0.45	91	1.88	This work

^[a] The potential reported at photocurrent density of 0.5 mA cm⁻².

^[b] The highest FE reported in the system.

^[c] Calculated using equation 7 in Methods Section.

Table S4. Performance comparison of recent state-of-the-art catalysts for (photo)electrochemical CO₂ reduction into CO. Related to Figure 3.

Catalytic architecture	Potential	TOF (h ⁻¹)	Refs.
Ag/Si NWs	-1.4 V vs. RHE	2400	Wei et al., 2019
Single Sb/NC	-0.9 V vs. RHE	16600	Jia et al., 2019
Single Ni/graphene	2.78 V vs. RHE	210000	Jiang et al., 2018
Ni ^I -NCNT@Ni ₉ Cu	-0.73 V vs. RHE	1962	Zhang et al., 2020
NC-CNTs (Ni)	-1.0 V vs. RHE	11650	Fan et al., 2019
PyNiPc	-0.93 V vs. RHE	13000	Ma et al., 2020
Cr(^{tBu} dhbpy)Cl(H ₂ O)	-0.22 V vs. RHE	20520	Hooe et al., 2019
Fe-TPP-Dimer/CNT	-0.88 V vs. RHE	36000	Abdinejad et al., 2020
<i>meta</i> -Re(bpy)(CO) ₃ Cl	-1.98 V vs. Fc ⁺⁰	860400	Talukdar et al., 2020
AuPt/GaN/n <sup+< sup="">-p Si</sup+<>	0.17 V vs. RHE	56400	This work

Reference:

Abdinejad, M., Dao, C., Deng, B., Sweeney, M.E., Dielmann, F., Zhang, X., and Kraatz, H.B. (2020). Enhanced electrochemical reduction of CO₂ to CO upon immobilization onto carbon nanotubes using an iron-porphyrin dimer. *ChemistrySelect* *5*, 979-984.

Blöchl, P. E. (1994) Projector augmented-wave method. *Phys. Rev. B* *50*, 17953.

Chu, S., Fan, S. Z., Wang, Y. J., Rossouw, D., Wang, Y. C., Botton, G. A., and Mi, Z. (2016) Tunable syngas production from CO₂ and H₂O in an aqueous photoelectrochemical cell. *Angew. Chem. Int. Ed.* *55*, 14260-14264.

Chu, S., Ou, P., Ghamari, P., Vanka, S., Zhou, B., Shih, I., Song, J., and Mi, Z. (2018) Photoelectrochemical CO₂ reduction into syngas with the metal/oxide interface. *J. Am. Chem. Soc.* *140*, 7869-7877.

Deng, X., Li, R., Wu, S., Wang, L., Hu, J., Ma, J., Jiang, W., Zhang, N., Zheng, X., Gao, C., Wang, L., Zhang, Q., Zhu, J., and Xiong, Y. (2019) Metal-organic framework coating enhances the performance of Cu₂O in photoelectrochemical CO₂ reduction. *J. Am. Chem. Soc.* *141*, 10924-10929.

Fan, Q., Hou, P., Choi, C., Wu, T.S., Hong, S., Li, F., Soo, Y.L., Kang, P., Jung, Y., and Sun, Z. (2019). Activation of Ni particles into single Ni–N atoms for efficient electrochemical reduction of CO₂. *Adv. Energy Mater.* *10*, 1903068.

Hooe, S.L., Dressel, J.M., Dickie, D.A., and Machan, C.W. (2019). Highly efficient electrocatalytic reduction of CO₂ to CO by a molecular chromium complex. *ACS Catal.* *10*, 1146-1151.

Jang, Y. J., Jeong, I., Lee, J., Lee, J., Ko, M. J., Lee, J. S. Unbiased sunlight-driven artificial photosynthesis of carbon monoxide from CO₂ using a ZnTe-based photocathode and a perovskite solar cell in tandem. *ACS Nano* **2016**, *10*, 6980.

Jia, M., Hong, S., Wu, T.-S., Li, X., Soo, Y.-L., and Sun, Z. (2019). Single Sb sites for efficient electrochemical CO₂ reduction. *Chem. Commun.* **55**, 12024-12027.

Jiang, K., Siahrostami, S., Zheng, T., Hu, Y., Hwang, S., Stavitski, E., Peng, Y., Dynes, J., Gangisetty, M., Su, D., *et al.* (2018). Isolated Ni single atoms in graphene nanosheets for high-performance CO₂ reduction. *Energy Environ. Sci.* **11**, 893-903.

Kim, T.W., and Choi, K.S. (2014). Nanoporous BiVO₄ photoanodes with dual-layer oxygen evolution catalysts for solar water splitting. *Science* **343**, 990-994.

Kobayashi, H., Sato, N., Orita, M., Kuang, Y., Kaneko, H., Minegishi, T., Yamada, T., and Domen, K. (2018). Development of highly efficient CuIn_{0.5}Ga_{0.5}Se₂-based photocathode and application to overall solar driven water splitting. *Energy Environ. Sci.* **11**, 3003-3009.

Kong, Q., Kim, D., Liu, C., Yu, Y., Su, Y., Li, Y., and Yang, P. D. (2016) Directed assembly of nanoparticle catalysts on nanowire photoelectrodes for photoelectrochemical CO₂ reduction. *Nano Lett.* **16**, 5675-5680.

Kresse, G., and Furthmüller, J. (1996) Efficiency of ab-initio total energy calculations for metals and semiconductors using a plane-wave basis set. *Comput. Mater. Sci.* **6**, 15.

Kresse, G., and Hafner, J. (1994) Ab initio molecular-dynamics simulation of the liquid-metal–amorphous-semiconductor transition in germanium. *Phys. Rev. B* **49**, 14251.

Kresse, G., and Joubert, D. (1999) From ultrasoft pseudopotentials to the projector augmented-

wave method. *Phys. Rev. B* *59*, 1758.

Li, C. C., Wang, T., Liu, B., Chen, M. X., Li, A., Zhang, G., Du, M. Y., Wang, H., Liu, S. F., and Gong, J. L. (2019) Photoelectrochemical CO₂ reduction to adjustable syngas on grain-boundary-mediated a-Si/TiO₂/Au photocathodes with low onset potentials. *Energy Environ. Sci.* *12*, 923-928.

Li, H., Wen, P., Itanze, D. S., Hood, Z. D., Ma, X., Kim, M., Adhikari, S., Lu, C., Dun, C., Chi, M., et al. (2019) Colloidal silver diphosphide (AgP₂) nanocrystals as low overpotential catalysts for CO₂ reduction to tunable syngas. *Nat. Commun.* *10*, 5724.

Li, L., Mu, X., Liu, W., Kong, X., Fan, S., Mi, Z., and Li, C. (2014) Thermal non-oxidative aromatization of light alkanes catalyzed by gallium nitride. *Angew. Chem. Int. Ed.* *53*, 14106.

Ma, D.-D., Han, S.-G., Cao, C., Li, X., Wu, X.-T., and Zhu, Q.-L. (2020). Remarkable electrocatalytic CO₂ reduction with ultrahigh CO/H₂ ratio over single-molecularly immobilized pyrrolidinonyl nickel phthalocyanine. *Appl. Catal. B* *264*, 118530.

Monkhorst, H. J., and Pack, J. D. (1976) Special points for brillouin-zone integrations. *Phys. Rev. B* *13*, 5188.

Nørskov, J. K., Rossmeisl, J., Logadottir, A., Lindqvist, L., Kitchin, J. R., Bligaard, T., and Jonsson, H. (2004) Origin of the overpotential for oxygen reduction at a fuel-cell cathode. *J. Phys. Chem. B* *108*, 17886.

Sheng, W., Kattel, S., Yao, S., Yan, B., Liang, Z., Hawxhurst, C. J., Wu, Q., and Chen, J. G. (2017) Electrochemical reduction of CO₂ to synthesis gas with controlled CO/H₂ ratios. *Energy Environ. Sci.* *10*, 1180.

Song, J. T., Ryoo, H., Cho, M., Kim, J., Kim, J. G., Chung, S. Y., and Oh, J. (2017) Nanoporous Au Thin Films on Si Photoelectrodes for Selective and Efficient Photoelectrochemical CO₂ Reduction. *Adv. Energy Mater.* *7*, 1601103.

Sui, M., Li, M. Y., Kim, E. S., and Lee, J. (2013) Annealing temperature effect on self-assembled Au droplets on Si (111). *Nanoscale Res. Lett.* *8*, 525.

Talukdar, K., Sinha Roy, S., Amatya, E., Sleeper, E.A., Le Magueres, P., and Jurss, J.W. (2020). Enhanced electrochemical CO₂ Reduction by a series of molecular rhenium catalysts decorated with second-sphere hydrogen-bond donors. *Inorg. Chem.* *59*, 6087-6099.

Tripković, V., Skúlason, E., Siahrostami, S., Nørskov, J. K., and Rossmeisl, J. (2010) The oxygen reduction reaction mechanism on Pt(111) from density functional theory calculations. *Electrochimi. Acta* *55*, 7975.

Vanka, S., Arca, E., Cheng, S., Sun, K., Botton, G. A., Teeter, G., and Mi, Z. (2018) High efficiency Si photocathode protected by multifunctional GaN nanostructures. *Nano Lett.* *18*, 6530.

Wei, L., Lin, J., Xie, S., Ma, W., Zhang, Q., Shen, Z., and Wang, Y. (2019). Photoelectrocatalytic reduction of CO₂ to syngas over Ag nanoparticle modified p-Si nanowire arrays. *Nanoscale* *11*, 12530-12536.

Wellendorff, J., Lundgaard, K. T., Møgelhøj, A., Petzold, V., Landis, D. D., Nørskov, J. K., Bligaard, T., and Jacobsen, K. W. (2012) Density functionals for surface science: Exchange-correlation model development with bayesian error estimation. *Phys. Rev. B* *85*, 235149.

Zhang, T., Han, X., Yang, H., Han, A., Hu, E., Li, Y., Yang, X.q., Wang, L., Liu, J., and Liu, B. (2020). Atomically dispersed nickel(I) on an alloy-encapsulated nitrogen-doped carbon

nanotube array for high-performance electrochemical CO₂ reduction reaction. *Angew. Chem. Int. Ed.* doi.org/10.1002/anie.202002984.